ORIGINAL RESEARCH ARTICLE

The Role of Boron in Low Copper Spheroidal Graphite Irons

A.V. BUGTEN, L. MICHELS, R.B. BROROK, C. HARTUNG, E. OTT, L. VINES, Y. LI, L. ARNBERG, and M. DI SABATINO

The effects of boron at concentrations ranging from 5 to 525 ppm in low copper spheroidal graphite iron (SGI) has been studied. At 130 to 140 ppm, no particular effect of boron was observed on the size distributions, number densities, or morphologies of the microparticle populations in the material. Neither was there observed any effects on the size distributions or number densities of graphite nodules. However, boron was observed to lead to a rough surface morphology of the graphite nodules at concentrations as small as 24 ppm. Intercellular carbides were found to form in alloys containing more than 70 ppm boron. Additionally, the graphite shape began to degenerate in alloys with more than 300 ppm of boron. Mass spectrometry analyses revealed these carbides contain relatively high amounts of boron. In an alloy containing 74 ppm boron, it was inferred by using electron backscatter diffraction that these were of the type $M_{23}(C, B)_6$ borocarbides, where M = Fe, Mn, V, or a combination of them. Mass spectrometry analyses also revealed elevated concentrations of boron in the surface layers of the graphite nodules.

https://doi.org/10.1007/s11661-023-07014-y

I. INTRODUCTION

SPHEROIDAL graphite iron (SGI) is a type of cast iron characterized by a spherical shape of the graphite. To obtain a high quality casting, one must optimize the morphology and size distribution of graphite, the number density of graphite nodules, the phase fractions, and the amount of microstructural constituents such as microparticles and inclusions.[1,2] This is further achieved by having good control of temperature, chemical composition, melt treatment, and holding time before pouring, and cooling conditions after pouring.[2–4] Here, melt treatment includes preconditioning, nodularization, and inoculation. The cooling conditions after pouring are important for the microstructure because they affect the phases that precipitate, graphite nodule number density, graphite morphology, and phase fractions.[5] Spheroidal graphite is precipitated in stable conditions during solidification, *i.e.* according to the stable iron-carbon phase diagram. If the cooling is fast, or the melt is uninoculated, carbon may also precipitate as the iron-carbide known as cementite (Fe_3C), according to the metastable iron-cementite phase diagram.

The chemical composition of an SGI alloy has a profound effect on the microstructure of the material. Silicon is a graphitizer, meaning that precipitation of graphite is favored over precipitation of carbides with increasing Si content. Free sulfur and oxygen promote lamellar graphite, which must be prevented in order to obtain SGI. Some elements (*e.g.* B, Cr, V, Mo, Mn) promote carbides, while other elements (*e.g.* Si, Al, Cu, and Ni) act as graphitizers. The pearlite/ferrite ratio can be controlled by adding Cu, Mn, Sn, or Sb, all of which promote formation of pearlite. Elements that deteriorate the graphite shape (*e.g.* S, O, Ti, Pb, Sb) are called subversive elements. Spheroidizing elements promote formation of spherical graphite. Examples of these elements are Mg, Ce, and La, and are extensively used to produce FeSi-based spheroidizers. Some elements aid the precipitation of graphite in the liquid by promoting heterogeneous nucleation. Examples of elements that

A. V. BUGTEN is with the Department of Materials Science and Engineering, Norwegian University of Science and Technology (NTNU), 7034 Trondheim, Norway. Contact: andreas.v.bugten@ntnu.no L. MICHELS is with the Innovation Department, Elkem Silicon Products (ESP), 4621 Kristiansand, Norway and also with the Department of Physics, Norwegian University of Science and Technology (NTNU), 7034 Trondheim, Norway. Contact: leander.michels@elkem.com; leander.michels@ntnu.no R. B. BROROK, Y. LI, L. ARNBERG, and M. DI SABATINO are with the Department of Materials Science and Engineering, Norwegian University of Science and Technology (NTNU). Contact: marisa.di.sabatino@ntnu.no C. HARTUNG, and E. OTT are with the Innovation Department, Elkem Silicon Products (ESP). L. VINES is with the Department of Physics/Centre for Materials Science and Nanotechnology, University of Oslo, 0318 Oslo, Norway.

Manuscript submitted October 28, 2022; accepted February 10, 2023.

Article published online May 10, 2023

possess such abilities are Ca, Al, Zr, Ba, Sr, and Ce. They are used to produce FeSi-based inoculants.[3,5,6]

Cast iron is often produced using steel scrap in combination with pig iron and cast iron returns, to lower the cost and carbon footprint of the material.[7–9] Boron (B) is frequently used in steels to increase the hardenability and wear resistance. This makes B containing steels an attractive material in several sectors, such as in the automotive and agricultural industries.[10,11] It is reported in several studies that B has detrimental effects on the microstructure and properties of cast irons, even at trace levels.[12–14] In cast iron, B is known to be one of the most potent carbide stabilizing elements, resulting in intercellular carbides when the bulk concentration of B is as low as 20 ppm.[5] Furthermore, B is known to promote formation of ferrite in pearlitic SGI alloyed with Cu.[15,16] Regarding the effects of B on graphite nodule number density, there are contradicting results reported in the literature. Kasvayee *et al*. and Izui *et al*. report no effect of B on nodule number density,[16,17] Guerra *et al*. report a decrease in nodule number density with increasing B content,[18] and Mitra *et al*. report an increase in nodule number density in SGI pipes.[19]

No effective method for neutralizing or removing B from the melt is currently known. Zou *et al*., managed to decrease the ferrite fraction by approximately 7 pct in boron-containing pearlitic copper-alloyed SGI (~1 wt pct Cu) by alloying with Ti, while the recovered pearlite fraction was less using nitrogen.[15] These pearlite fraction recoveries are not sufficient if a fully pearlitic matrix is desired. The preferred method of handling the effect of B in SGI is, therefore, to choose raw materials that are low in B.

In the current investigation into the role of B in SGI, the emphasis was on the effects of B in SGI alloys with low concentrations of Cu. The boron content has been varied systematically from lower levels that can be expected to arise in foundries, to concentrations that exceed what is expected. To avoid any complications introduced by rare earth elements (*e.g*. Ce and La) and Ba, nodularizers and inoculants that are low in these elements have been used. Previously conducted research on the effects of B in SGI has largely focused on graphite morphology, nodule number density, phase fractions, and mechanical properties.[15,16,18–20] The focus of this study was on the influence of B on the graphite and entire microparticle population, employing a combined back scattered electron (BSE) and energy dispersive spectroscopy (EDS) approach for particle detection and analysis, and a method for converting area number density to volume number density.[6,21] Furthermore, B was located in the microstructure by the use of secondary ion mass spectrometry (SIMS), and electron backscatter diffraction (EBSD) was employed for phase determination.

II. METHODS

A. *Materials*

A series of SGI alloys that differ in boron concentration have been prepared. Both alloys high in ferrite (70 to 80 pct ferrite) and alloys with mixed ferritic and pearlitic matrix (40 to 50 pct ferrite) have been studied. Mn was added to promote pearlite. The composition of the spheroidizer and inoculant can be found in Table I.

B. *Preparation of Alloys*

For each trial series 100 pct low alloyed cast iron returns were melted in a 275 kg induction furnace. Calibration of the alloy compositions were done by adding graphite (99.9 pct C) and FeMn (75 pct Mn) into the furnace. At approximately 1500 °C the alloys were transferred into a ladle containing 1.2 wt pct of nodularizer. The capacity of the ladle was 275 kg. The melts were then poured into six alumina crucibles with 0.2 wt pct of inoculant inside. The crucibles also contained varying amounts of FeB to achieve the correct B level in the samples. The capacity of each crucible was 32 kg. The final iron compositions are given in Table II. The measured concentrations of B in alloys Fe-B_4 and M-B_5 are likely the background level measured by the spark optical emission spectrometer.

After inoculation, a chill coin was collected from each crucible for determination of the chemical composition. The remaining liquids in the crucibles were subsequently poured into horizontal molds for cylindrical tensile bars with diameter 30 mm after a holding time of one minute. The cylindrical bars were later used to evaluate microstructure.

The pouring temperatures were measured to be around 1400 °C for the various samples. A temperature difference of 30 °C was observed from the first to the last of the six samples per trial.

The bulk chemical composition of each sample was obtained through analyzing the chill coins in a spark optical emission spectrometer (ARL ispark 8860). To determine the bulk concentration of O, N, and C more accurately, a part of the chill coins was also analyzed using combustion techniques. A Leco ON836 was employed for N and O, and a Leco ON844 was employed for C. The carbon equivalent (CE) is calculated according to: CE = wt pct C + 0.31 · wt pct Si + 0.33 · wt pct P - 0.029 · wt pct Mn + 0.41 · wt pct S.[12] The sample identification tags used in this study is comprised of a letter to indicate whether the sample matrix is predominantly ferritic (”F”), or a mix of approximately 50 pct ferrite and 50 pct pearlite (”M”). The amount of boron in ppm in the alloy is given by ”B_X”, where ”X” denotes the B level, *e.g*. sample M-B_{140} has a matrix consisting of a mix of ferrite and pearlite, and contains 140 ppm B.

C. *Microstructure Characterization*

Standard metallographic techniques (*i.e*. grinding and polishing down to $\frac{1}{4}$ μm) were utilized to prepare samples for optical microscopy (OM), scanning electron

Table I. The Composition of the Employed Spheroidizer and Inoculant, Both of Which are FeSi Alloys

Alloy	Type	Si [wt pct]	Ca [wt pct]	Al [wt pct]	Mg [wt pct]	Ce [wt pct]	C [wt pct]	O [wt pct]
(Mg)-FeSi	Nodularizer	45.8	1.5	0.7	5.9	0.17	< 0.05	< 0.2
(Ca,Al)-FeSi	Inoculant	76.0	1.2	1.4	—	—	< 0.05	< 0.2

The balance is Fe.

Table II. The Bulk Chemical Composition for the Most Relevant Alloys

Sample ID	C [wt pct]	Si [wt pct]	Mn [wt pct]	Mg [wt pct]	Al [wt pct]	O [wt pct]	S [wt pct]	N [wt pct]	Ce [wt pct]	Cu [wt pct]	CE [wt pct]	B [ppm]
F-B_4	3.56	2.50	0.137	0.047	0.0110	0.0012	0.0076	0.0049	0.0046	0.019	4.34	4
F-B_24	3.50	2.56	0.137	0.049	0.0110	0.0002	0.0075	0.0046	0.0046	0.019	4.29	24
F-B_{74}	3.51	2.49	0.138	0.048	0.0110	0.0005	0.0073	0.0047	0.0044	0.019	4.29	74
F-B_{130}	3.55	2.49	0.138	0.046	0.0100	0.0001	0.0078	0.0045	0.0041	0.019	4.33	130
F-B_{330}	3.47	2.39	0.123	0.046	0.0096	0.0005	0.0086	0.0053	0.0035	0.018	4.22	330
F-B_{525}	3.46	2.45	0.123	0.044	0.0096	0.0003	0.0085	0.0051	0.0033	0.017	4.22	525
M-B_5	3.50	2.33	0.667	0.045	0.0100	0.0002	0.0075	0.0046	0.0053	0.021	4.21	5
M-B_{73}	3.41	2.31	0.662	0.046	0.0100	0.0003	0.0081	0.0044	0.0042	0.020	4.11	73
M-B_{140}	3.38	2.31	0.664	0.043	0.0097	0.0001	0.0078	0.0043	0.0043	0.020	4.08	140
M-B_{310}	3.49	2.20	0.659	0.046	0.0088	0.0004	0.0080	0.0054	0.0026	0.015	4.16	310
M-B_{525}	3.39	2.24	0.660	0.045	0.0090	0.0005	0.0083	0.0052	0.0033	0.015	4.07	525

CE carbon equivalent. F = high in ferrite, M = mixed grade. Concentrations of other notable elements are Zr (less than 0.0009 wt pct), La (ca. 0.0011 wt pct), P (ca. 0.0014 wt pct), V (ca. 0.018 wt pct), Nb (ca. 0.0013 wt pct), Ti (ca. 0.0039 wt pct), Cr (ca. 0.029 wt pct).

microscopy (SEM), and secondary ion mass spectrometry (SIMS). Additionally, to reveal the matrix phases for OM, some of the samples were etched for 15 seconds in 2 pct Nital. The samples were cut from the center of the cross section of the cast bars to ensure representative and comparable results.

The OM used for microstructure evaluation was a Zeiss Axioplan 2. The magnification was 100 times. The phase fractions, nodule number density, and nodularity, were determined by employing a method based on ASTM E2567-16a, utilizing a Micropublisher 5.0 RTV digital camera. The area evaluated per sample was 14.2 mm^2. A minimum nodule diameter cut-off size of 5 μm was used in the counting procedure. The image size was 1280x960 pixels, and the image resolution was 0.68 μm/pixel.

For the SIMS analyses a Cameca IMS 7f instrument was employed. The primary ion beam was 10 keV O_2^+, and a current of 10 nA was used during elemental distribution mapping. To remove surface impurities, the sample areas of interest were presputtered for 2 minutes with the current set to 300 nA.

To map the microparticle population of the samples an automated BSE/EDS method was employed, using the Automated Mineral Identification and Characterization System (AMICS). The SEM was a Zeiss Merlin Compact, and the EDS detector was a Bruker XFlash 6130. The microparticle population was measured in an area of 6.27 mm^2. To avoid large uncertainties regarding particle size and chemical composition, the minimum particle size was set to 0.5 μm^2.

For EBSD, a Zeiss ULTRA 55 LE FE-SEM was used. The software utilized to capture the EBSD data was NORDIF. The data was subsequently processed in kikuchipy.[22] EMsoft[23,24] was used to simulate the Lambert projection for various phases to compare with the experimental EBSD data.

D. *Particle Number Density and Size Distribution*

To estimate the particle number density (per mm^3) and size distribution of the graphite nodules and microparticles, a Finite Difference Method (FDM) for conversion from 2D to 3D number densities was utilized.[21] This method is similar to the Schwartz-Saltykov model,[25,26] where the 2D size distribution is divided into k class intervals of size Δ, but the present model assumes a continuous size distribution instead of a discrete size distribution. Once the microparticles are arranged in k size classes the number of particles per mm^2, $N_A(i)$, in each respective class can be found. The size interval of the classes are $(i - 1)\Delta$ to $i\ \Delta$, i being a positive integer between 1 and k. The volumetric number density, $N_V(j)$, is then calculated according to:

$$N_V(j) = \Delta^{-1} \sum_{i=j}^{k} \alpha(i,j) N_A(i) \quad [1]$$

The coefficients $\alpha(i,j)$ are determined through[21]:

$$\alpha(i,j) = \frac{2}{\pi} \ln \left[\frac{i + \sqrt{i^2 - (j-1)^2}}{i + \sqrt{i^2 - j^2}} \cdot \frac{i - 1 + \sqrt{(i-1)^2 - j^2}}{i - 1 + \sqrt{(i-1)^2 - (j-1)^2}} \right] \forall\ (i > j) \quad [2]$$

and for the cases where i equals j:

$$\alpha(j,j) = \begin{cases} 1 & (i=j) \\ \frac{2}{\pi}\ln\left[\frac{j+\sqrt{j^2-(j-1)^2}}{j-1}\right] & \forall\ (j>1), \end{cases} \quad [3]$$

Finally, by summing $N_V(j)$ for the individual size classes, one can determine the volumetric number density:

$$N_{V\text{total}} = \sum_{j=1}^{k} N_V(j) \quad [4]$$

The interval size Δ in Eq. [1] (also known as bandwidth, *h*), should not be an arbitrary number. Both the accuracy of variations of the Saltykov method (such as the FDM code applied in the current study) and the accuracy of histograms rely on a suitable choice for the interval size. The interval size is often calculated as the difference between maximum and minimum particle size (*d*) divided by the number of size classes *k*:

$$\Delta = \frac{d_{max} - d_{min}}{k} \quad [5]$$

The N_V values can be plotted as a function of feret diameter, thereby showing the size distribution as a histogram. A log-normal function can then be fitted to the size distribution according to:

$$\frac{dn}{d\phi} = \frac{n_{max}}{\phi_\sigma\sqrt{2\pi}}\frac{1}{\phi}\exp\left[-\frac{1}{2}\left(\frac{\ln\phi - \ln\phi_o}{\phi_\sigma}\right)^2\right] \quad [6]$$

where $dn/d\phi$ is the particle density in mm^{-3}; ϕ is the diameter; n_{max} is the maximum number density; ϕ_o is the mean diameter, and ϕ_σ is the standard deviation.

If the size distribution for a sample is bimodal, two different log-normal functions can be fitted to represent the size distribution.

E. *Thermodynamic Calculations*

The CALPHAD-based software FactSage version 8.2[27] was used to compute the Fe-B phase diagram presented in Figure 5(a). The database FSteel was chosen for the calculations. The classic Scheil simulation for segregation of B in a liquid Fe-$C_{3.5}$-$Si_{2.3}$-$Mn_{0.137}$-$B_{0.01}$ alloy was performed in Thermo-Calc version 2022a using TCFE12 Steels/Fe-alloys Database.[28]

III. RESULTS

A. *Influence of Boron on the Microstructure*

A series of micrographs showing the evolution of microstructure with increasing boron content for the ferritic and mixed grades are presented in Figure 1. As can be seen, at a B concentration of 73 ppm, a carbide phase appears within the pearlitic regions, as shown by the red arrow in Figure 1(d). Increasing the B content in the alloy also increases the area fraction of this phase. Notably, the ferrite fraction does not seem to decrease as the carbide phase grows (fraction of ferrite, pearlite, graphite and carbide sums to 100 pct).

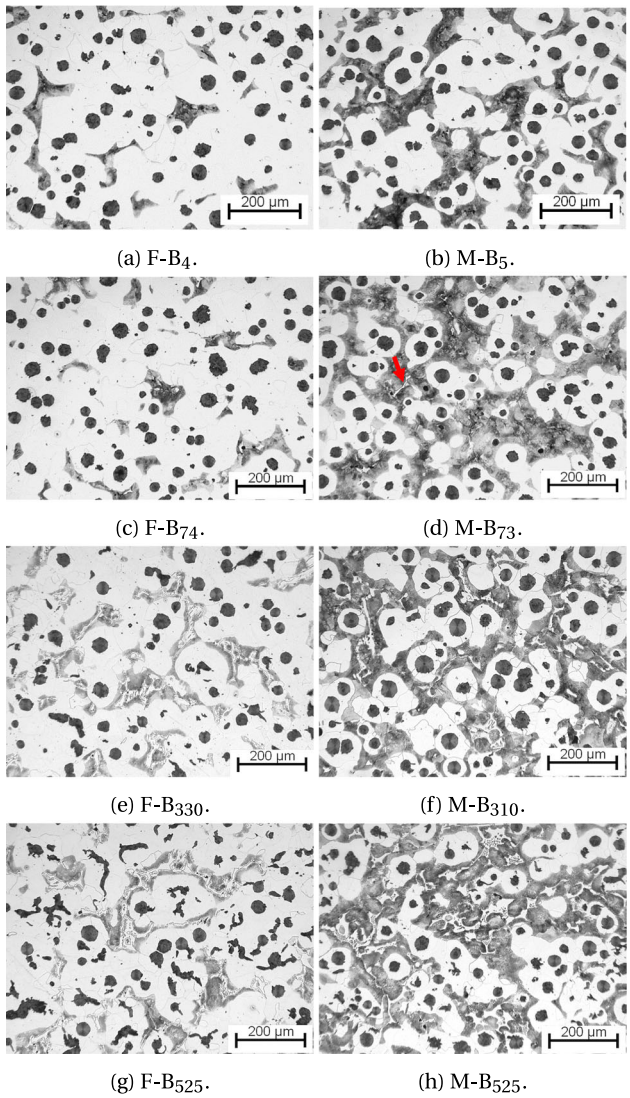

(a) F-B_4. (b) M-B_5.
(c) F-B_{74}. (d) M-B_{73}.
(e) F-B_{330}. (f) M-B_{310}.
(g) F-B_{525}. (h) M-B_{525}.

Fig. 1—Microstructure evolution of the ferritic samples in the left column [(*a*), (*c*), (*e*), and (*g*)], and the mixed grade samples in the right column [(*b*), (*d*), (*f*), and (*h*)]. The amount of boron increases between each micrograph from top to bottom in the columns. The boron concentration is given in the sample identity beneath each respective micrograph.

Nodule number density (per unit area), nodularity, and fractions of ferrite and graphite were determined from these micrographs. The results are presented in Figure 2. At B concentrations below 300 ppm, the area number density of nodules is stable, Figure 2(a). From approximately 300 ppm, a sharp decrease in nodule number density correlates with a sharp decrease in nodularity [Figure 2(b)]. This is because the method used to determine nodule number density (ASTM E2567-16a) only takes graphite nodules with a nodularity above 60 pct into account. The measured nodularities of the alloys are observed to decrease from approximately 300 ppm B. The area fractions of ferrite

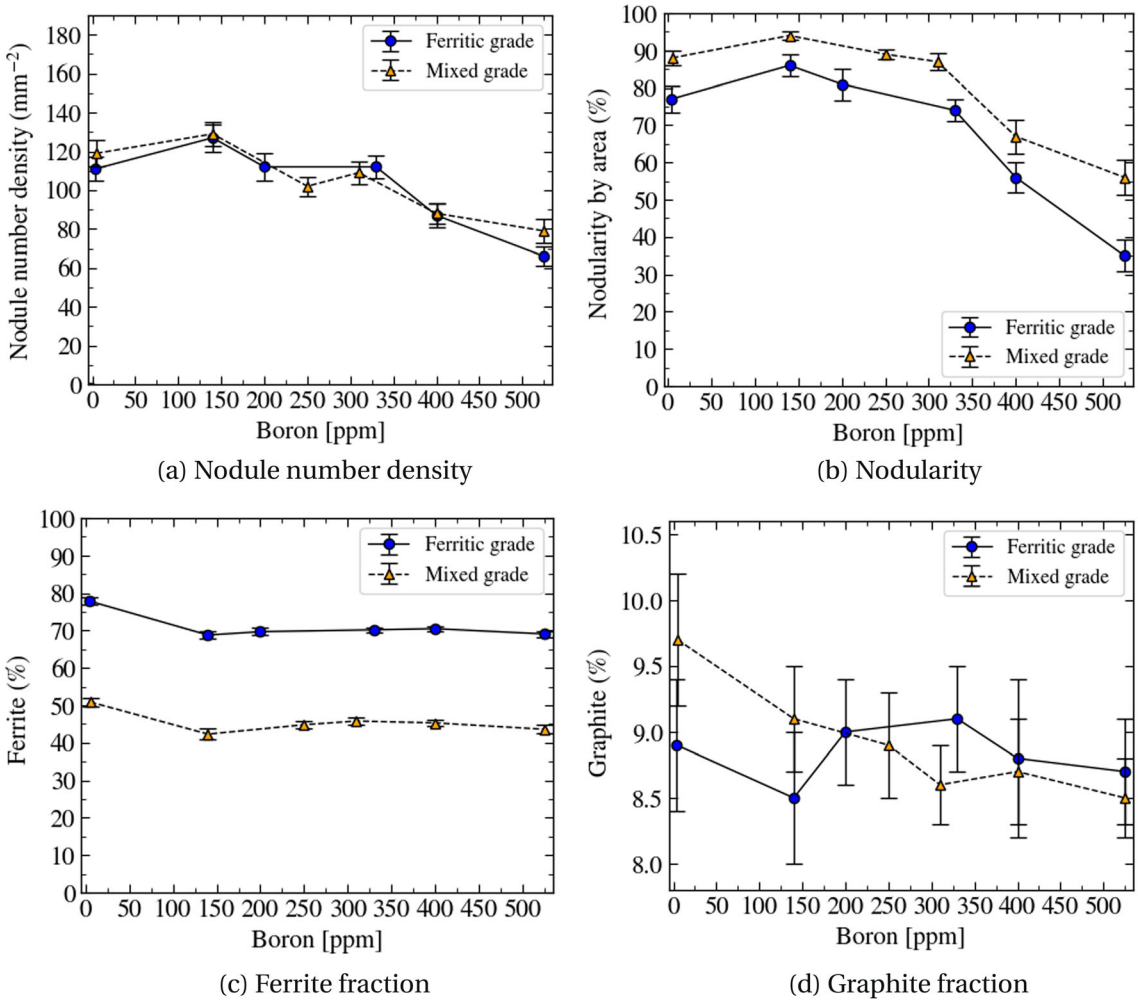

Fig. 2—The microstructure variables for the ferritic and mixed grade samples: (*a*) nodule number density; (*b*) nodularity; (*c*) ferrite fraction; (*d*) graphite fraction.

[Figure 2(c)] and graphite [Figure 2(d)] remain constant with increasing boron addition levels.

Observing the microstructure of sample F-B_{525}, Figure 1(g), it becomes apparent that only some graphite nodules are degenerated. Three forms of graphite can be observed: graphite nodules, intermediate graphite particles, and completely degenerated graphite particles. The intermediate graphite particles appear as graphite nodules with arms that branch out from the nodule. These graphite particles are known as tadpole graphite (TPG).[29] The completely degenerated form of graphite is reminiscent of compacted graphite (CG). Small amounts of degenerated graphite can also be seen in sample M-B_{310}.

It was observed a larger tendency for graphite nodules with rough surface morphologies in alloys with concentrations of B ranging from 24 ppm to 140 ppm compared to alloys with no additions of B. Figure 3 presents two graphite nodules from the alloys F-B_4 and F-B_{24}. The surface of the nodule from alloy F-B_4 is smooth, while the surface of the nodule from alloy F-B_{24} is rough.

Figure 4 shows magnified images of the carbide phase in sample F-B_{130}. The carbide is found within the pearlitic regions in the material. Various microparticles, such as oxide particles, can be observed in the carbide phase.

The Fe-B binary phase diagram, and a classic Scheil simulation of B in a Fe-$C_{3.5}$-$Si_{2.3}$-$Mn_{0.137}$-$B_{0.01}$ alloy are presented in Figure 5. The initial concentration of B in the Scheil simulation was 100 ppm.

B. *Characterization of the Carbide Phase*

Figure 6 shows some of the results from the SIMS analysis. Figure 6(a), shows what the microstructure of the analyzed area looks like in the SEM using the BSE-mode. The green rectangle shows the region of interest characterized with SIMS, see Figure 6(b) through (g). The distribution of C in the sample is presented in Figure 6(b). C mainly exists as graphite nodules. The distribution of B is presented in Figure 6(c). Here it is observed that B segregates to two locations. Firstly, most of the B segregates to areas

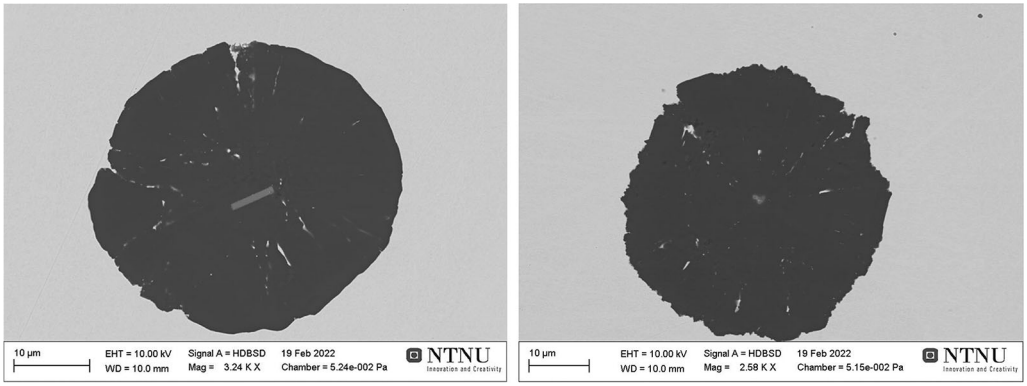

(a) (b)

Fig. 3—Examples of graphite nodule surface morphologies in alloys containing (*a*) 4 ppm B, and (*b*) 24 ppm B.

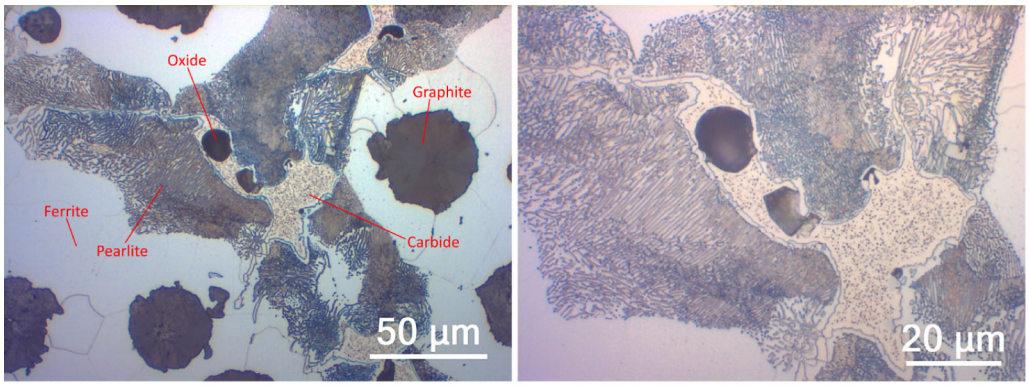

(a) (b)

Fig. 4—Microstructure of sample F-B_{130}. (*a*) Overview of the carbide phase within pearlite, with surrounding ferrite and graphite nodules. (*b*) Micrograph of the carbide phase.

in the matrix far from the graphite nodules. This indicates segregation towards the last-to-freeze regions. Secondly, some B is also found around or in the graphite nodules themselves. The segregation of B around nodules has been observed with SIMS by Izui *et al.*[30] The segregation of V coincides with the segregation of B in the matrix, as observed in Figure 6(e). A great number of microparticles can also be observed in the SIMS distribution map. See Figures 6(d), (f), and (g). These contain Mg, Ca, or Al, and could be (Ca,Mg)-sulfides and (Al,Si,Mg)-nitrides.

The area with high B concentration marked by the red rectangle in Figure 6(c), was examined with EDS and EBSD. Figure 7(a) shows an overview of the high B area. There, one can observe a bright phase that has a similar shape as the high B area in Figure 6(c) located by the red rectangle. A line scan was performed across the phase, as shown in Figure 7(b). The selected elements were Fe, C, and Si. The results are presented in Figure 7(c). Here, one can observe that the concentration of C increases in the phase, while the concentration of Si decreases. The concentration of Fe is approximately 90 wt pct across the phases, but the result for Fe is not shown in the line scan plot.

EBSD analysis was conducted to determine the chemical composition of the high B phase. The Kikuchi patterns for nine points were obtained along the phase. These Kikuchi patterns were subsequently processed in kikuchipy.[22] The Lambert projection for the face-centered cubic (fcc) phase $Fe_{23}(C,B)_6$ with space group *Fm-3m* (225), as well as the projections for ferrite and cementite, were then simulated in EMsoft. Using kikuchipy, the experimental Kikuchi patterns were compared with the best fit of the simulated pattern from EMsoft. The results are presented in Figure 8.

The materials parameters used for the simulations of the Lambert projections and the VESTA crystal structures are provided in Table 3.

C. *Influence of Boron on the Graphite and Microparticle Populations*

The graphite and microparticle populations were documented in a 6.27 mm^2 area of the polished sample

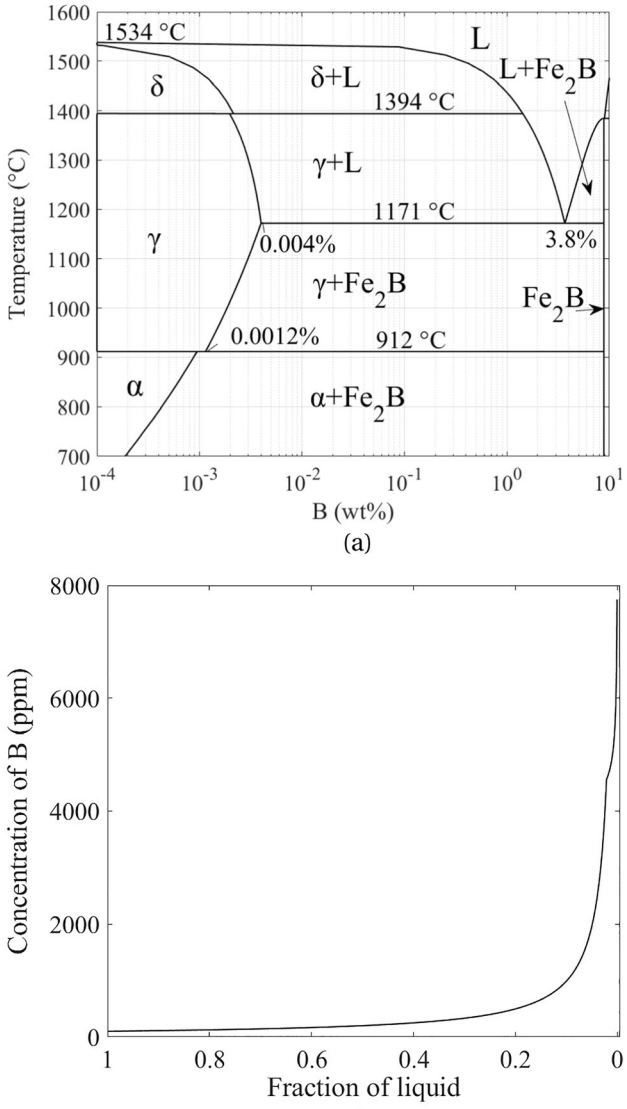

Fig. 5—(*a*) The Fe-B binary phase diagram, and (*b*) classic Scheil simulation showing the enrichment of B in the last-to-solidify liquid.

planes using AMICS. A BSE example image for sample F-B_{130} and a corresponding image showing the chemically classified regions (obtained with AMICS) are presented in Figure 9.

Magnesium was observed to be a key element in all the microparticle classes, except for the carbides. For the sulfides class, the predominant particle type was (Ca,Mg)-S, which is extensively described in literature.[35–38] Rod shaped (Al,Si,Mg)-N particles (in 2D) were the predominant nitride particles, and this particle type is also frequently reported in literature.[35,36,39–41] The main oxide particles found were (Mg)-O and (Mg)-P-O, as also reported by Michels *et al.*[6] The carbide particles observed are (Ti,Nb,V)-C phases.

In the current study, clustering of particles is not taken into account, such that all particles are counted individually. Furthermore, morphology is not considered when counting graphite particles.

Figure 10(a) shows the area number densities for graphite and the different classes of microparticles. Here, the area number densities of all the microparticlasses are observed to decrease with increasing B content, with the exception of nitrides. The number density of nitrides increases with increasing B content for the ferritic samples, while it decreases for the mixed grade samples. The morphologies of the nitride particles are presented in Figure 11. Furthermore, it can be observed that the area number densities of graphite are of a similar magnitude as the area number densities of sulfides.

When converting the area number densities (N_A) to volume (N_V), shown in Figure 10(d), the densities of the carbides increases with increasing B content. Also, the N_V of graphite are much lower compared to that of sulfides. The other trends are similar to what is observed in the 2D case.

Figures 10(b), (c), and (e) present the area fractions of graphite, microparticles (collectively), and microparticle classes (individually). In Figure 10(b), one can see that the area fraction of graphite decreases with increasing B content, despite the increasing number densities observed in Figure 10(d). The same can be observed for microparticles collectively, Figure 10(c), when comparing with the ferritic samples in Figure 10(d). However, for the mixed grades, the volume number density and area fractions of microparticles both decrease. With the exception of sulfides for the ferritic grades, and carbides for the mixed grades, the area fractions of the microparticle classes are all observed to decrease with increasing B content in Figure 10(e).

The size distributions of the graphite feret diameters for the samples studied with AMICS are presented in Figures 12(a) through (d). Log-normal functions have been fitted to the size distributions, employing Eq. [6]. Figure 12(e) compares the log-normal functions of the graphite size distributions.

The size distributions of graphite feret diameter, Figures 12(a) through (d), show bimodal shapes. This is typical for SGIs inoculated with (Ca,Al)-FeSi inoculants.[5] The first peak is the largest of the two peaks and is located at the smallest feret sizes. The apex of the second peak is lower and shifted towards larger feret diameters. Figure 12(e) compares all the size distributions for graphite.

The log-normal fits of the size distributions for the various microparticle classes are presented in Figure 13. Here, the size distributions are mostly unimodal. The exception is sample F-B_4 for nitrides [Figure 13(c)].

The log-normal fit for sulfides show that the number of sulfides is lower for the high B samples compared to the low B samples, while the particle size remains constant. The same trend is observed for oxides. Nitrides increase in number when comparing the ferritic high B sample with its low B counterpart (sample F-B_4). The trend is opposite for the mixed grade samples. The log-normal fits for carbides indicate a small increase in particle number for both grades of ductile cast iron. The positions of the apexes are approximately the same for all of the four samples.

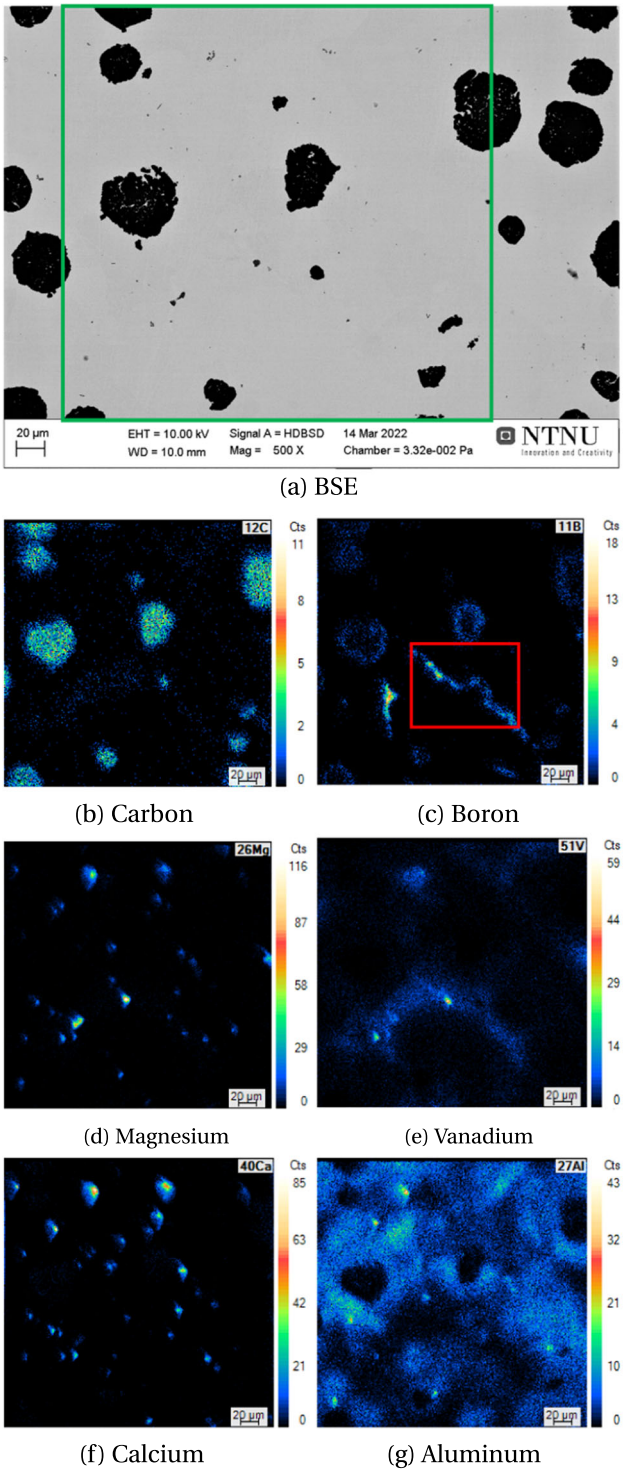

Fig. 6—SIMS of sample F-B_{74}. (*a*) The green rectangle highlights the area investigated in the SIMS. (*b*)–(*g*) The SIMS signals for C, B, Mg, V, Ca, and Al, respectively. In (b) the red rectangle shows the area later investigated with EBSD (Color figure online).

IV. DISCUSSION

A. *Distribution of Boron*

As shown by the micrographs in Figure 1 and the fraction of ferrite in Figure 2(c), there are no remarkable changes in fraction of ferrite with increasing concentration of B. Neither does the fraction of graphite change with increasing concentration of B. However, the carbide phase increases in area fraction with increasing concentration of B, as can be inferred from Figure 1.

The SIMS analysis showed that the carbide phase contained relatively large amounts of B. This suggests that segregation of B takes place during solidification. From the Fe rich part of the Fe-B phase diagram, Figure 5(a), it can be seen that γ-Fe has a low solubility of B (maximum 40 ppm in the binary Fe-B system). Furthermore, the classic Scheil simulation of B in an Fe-C-Si-Mn-B alloy, Figure 5(b), shows that B will become enriched in the last-to-solidify liquid.

Lenz *et al.* studied solidification and solid-state transformations of hypoeutectic Fe-B-C alloys.[42] Their research showed that for a hypoeutectic Fe-$C_{0.6}$-B alloy, $Fe_3(B,C)$ is formed during the eutectic transformation:

$$\text{Liquid} \rightarrow \gamma - \text{Fe} + \text{Fe}_2\text{B} + \text{Fe}_3(\text{B,C}) \qquad [7]$$

Upon further cooling, a peritectoid decomposition of $Fe_3(B,C)$ will occur for alloys with concentration of B below 1.5 wt% according to:

$$\text{Fe}_3(\text{B,C}) + \text{Fe} \rightarrow \text{Fe}_{23}(\text{C,B})_6 \qquad [8]$$

In the case of spheroidal graphite iron, where the concentration of C is substantially larger than the concentration of B, the eutectic reaction is likely:

$$\text{Liquid} \rightarrow \gamma - \text{Fe} + G + \text{Fe}_3(\text{C,B}) \qquad [9]$$

where G is graphite.

The formation of $Fe_{23}(C,B)_6$ starts with nucleation of a $Fe_{23}(C,B)_6$ crystal at the Fe-$Fe_3(C,B)$ interface, which then grows as the peritectoid transformation proceeds at the expense of the austenite and $Fe_3(C,B)$ phases. The $Fe_{23}(C,B)_6$ phase eventually forms a shell structure around the $Fe_3(C,B)$ phase. Further growth of the $Fe_{23}(C,B)_6$ phase relies on diffusion of B from the $Fe_{23}(C,B)_6/Fe_3(C,B)$ interface to the $Fe/Fe_3(C,B)$ interface, and the diffusion of C from either the Fe-matrix or the $Fe_3(C,B)$ phase to the Fe/ $Fe_{23}(C,B)_6$ interface.[42]

The observations from the SIMS, EDS, and EBSD analysis of the carbide phase fits this description well. It is revealed by employing SIMS that the carbide contains relatively high amounts of B. An increase in C concentration was documented by the line scan across the carbide phase, and the experimental Kikuchi patterns matched the best fit from the simulated Lambert projection of $Fe_{23}(C,B)_6$. The phase is not pure $Fe_{23}(C,B)_6$, since the SIMS analysis showed there was V present in the phase, and in the surrounding microstructure as well. Other elements not accounted for in the SIMS analysis can also be present, such as Mn. The observed carbide is therefore likely $M_{23}(C,B)_6$, where M = Fe, Mn, V or a blend of those.

The SIMS elemental mappings also showed elevated concentrations of B in the surface layers of the graphite nodules. The mechanism behind the segregation of B to

Table III. The Materials Parameters for the EMsoft Simulations and VESTA Crystal Structures

Phase	Space group	a [nm]	b [nm]	c [nm]	Wyckoff positions
α-Fe[31]	Im-3m (229)	0.287	0.287	0.287	Fe: 2a
Fe_3C[32]	Pnma (62)	0.509	0.674	0.453	Fe: 4c, 8d. C: 4c
$Fe_{23}(C,B)_6$[33,34]	Fm-3m (225)	1.046	1.046	1.046	Fe: 4b, 8c, 32f, 48 h. B: 24e. C: 4a

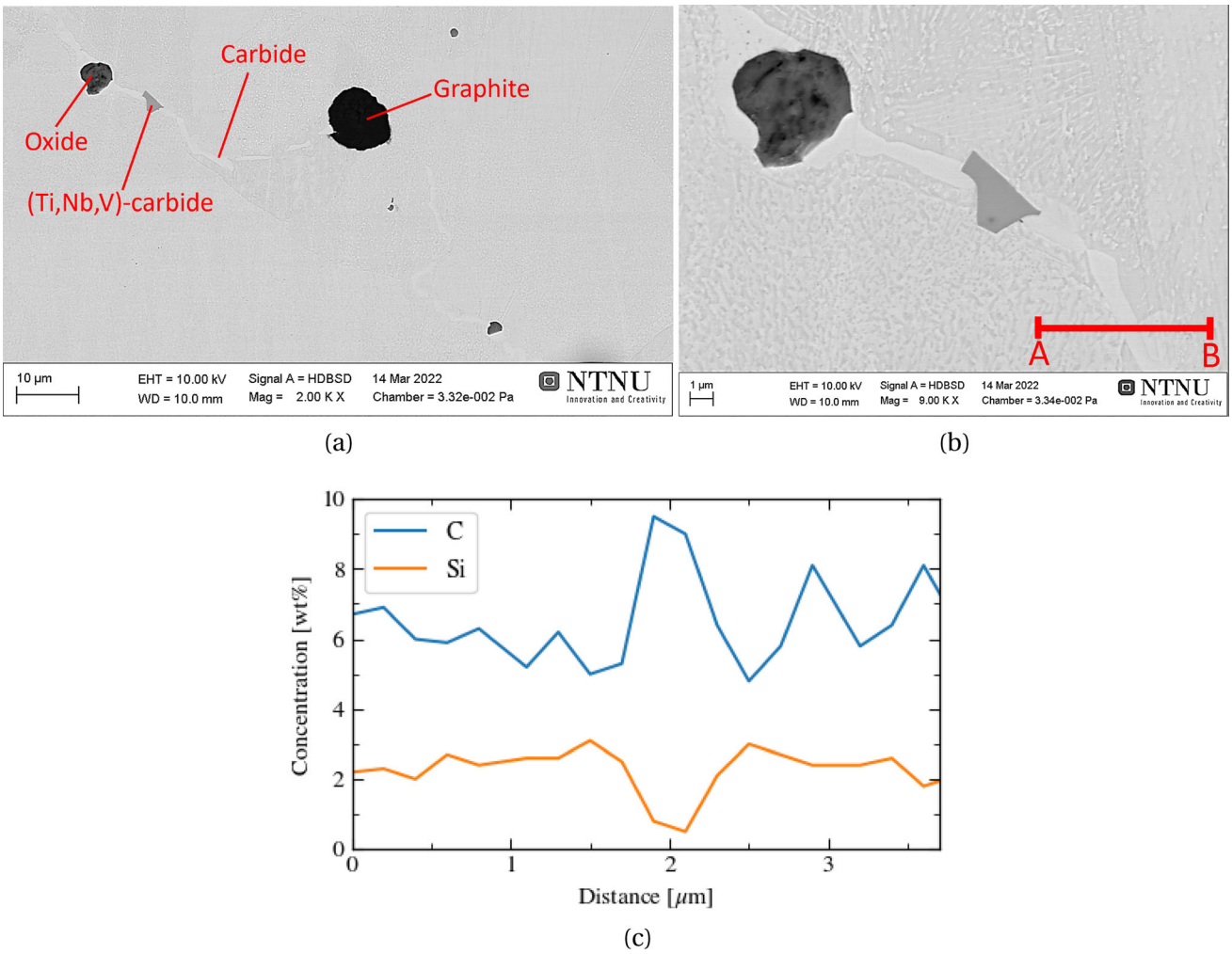

Fig. 7—(*a*) BSE image of high B area shown in Figure 6c. (*b*) The EDS line scan across the high B phase is marked by the red line from point A to point B. (*c*) The variation in C and Si across the carbide phase (Color figure online).

the graphite nodules is currently not understood. It may be related to primary growth of graphite, where B could be rejected into the melt, and subsequent solid-state diffusion of B.

B. *Graphite Shape*

Muhmond *et al.*[43] investigated the relationship between trace elements and graphite growth morphologies. The study showed that B atoms can attach to the basal plane in the graphite crystal structure. The B-C bonds are shorter than the C-C bonds, causing a strain in the lattice and a curvature of the basal plane. Compared to pure C atoms, the B doped basal plane has a higher energy. From this, the researchers concluded that B promotes flake growth of graphite in SGI.

Three types of graphite particles were observed in the microstructure of the samples where the B content was approximately 525 ppm (Figure 1). These are spherical graphite (SG), spherical graphite with one or more arms known as tadpole graphite (TPG), and completely degenerated graphite known as compacted graphite (CG). In a study on the effects of Pb on graphite shape by Tonn *et al.*[44] it was found that Pb lead to a similar

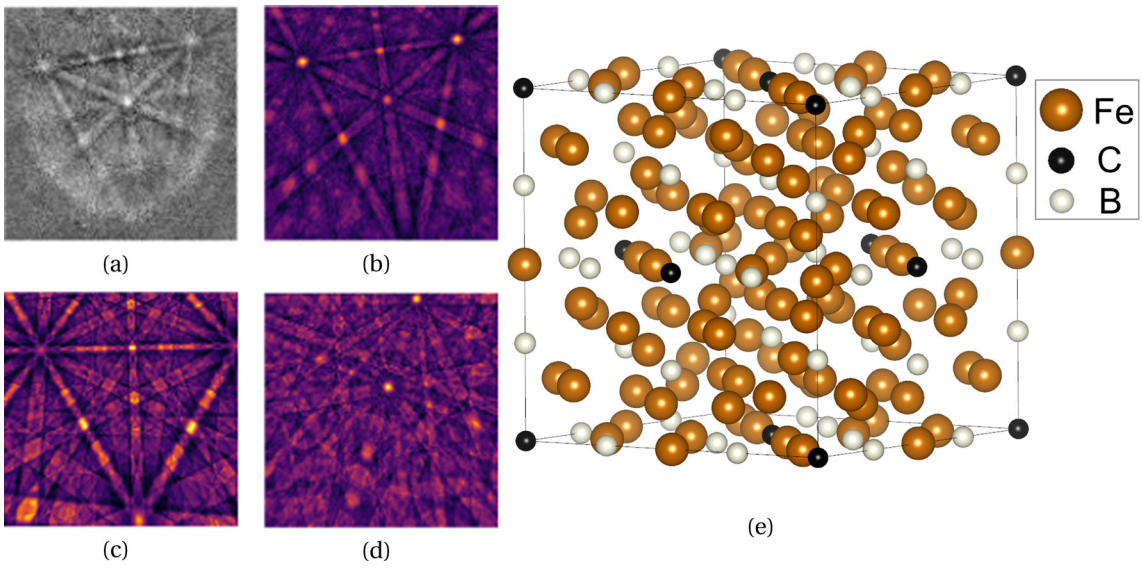

Fig. 8—(*a*) Example of an experimental Kikuchi pattern obtained from the boron containing carbide phase of sample F-B_{74}, see Figures 6(c) and 7(a). (*b*)–(*d*) Best fit to the experimental pattern from the simulated Lambert projection of $Fe_{23}(C,B)_6$, ferrite, and cementite, respectively. (*e*) Crystal structure of $Fe_{23}(C,B)_6$ obtained in VESTA. $Fe_{23}(C,B)_6$ has a fcc crystal structure with space group *Fm-3m* (225), while ferrite and cementite have bcc and orthorhombic crystal structures, respectively.

microstructure as to what is observed in the microstructure evolution in Figure 1. The researchers etched the sample with NaOH-CrO_3 and found that the fully degenerated graphite was found in the last-to-solidify regions of the microstructure. The TPG was found close to the last-to-solidify regions, and their arms extended towards the last-to-solidify regions. The graphite nodules were located further away from such regions.

From this information it may be deduced that the spherical graphite nucleate first, and has therefore nucleated in a melt less concentrated in B. When the solidification proceeds, the melt becomes enriched in B, leading to growth of TPG and eventually CG.

TPG is considered to be the first step in the SG-to-CG transition.[29] In a study by Stefanescu *et al.*[45] it was observed in interrupted solidification experiments that TPG was in most cases connected to cementite, while SG was surrounded by austenite. This suggests that TPG grows in contact with the liquid, while SG is quickly enveloped in an austenite shell. These observations support that the degenerated graphite particles in the current study are found in the regions that solidify later in the stages of solidification, where the B concentration is higher.

Concentrations of B below 300 ppm were found to influence the graphite nodule surface morphology. Additions of 24 ppm of B led to a rough surface morphology, as observed in Figure 3(b). This could be indicative of B being absorbed in the crystal structure of graphite and thereby affecting graphite growth.

C. *Particle Populations*

Generally, minor variations were observed in the total number densities for the various particles in 2D [Figure 8(a)]. The three largest differences in number densities between a high B sample and its low B counterpart was 55 pct, 27 pct and 20 pct, for nitrides, oxides, and graphite particles, respectively. For the remaining samples, the differences were all below 15 pct. The number density of graphite particles increases for both sample parallels, while the number densities of all microparticles decrease (with the exception of nitrides for the ferritic samples).

Nonmetallic microparticles are known to be favorable nuclei sites for graphite nodules.[37] These nonmetallic microparticles include sulfides, oxides, and nitrides. The measured amount of nitrides increases sharply for the ferritic samples in Figure 8(d). This is not observed for the mixed grade samples. Figure 9 suggests the nitride population in sample F-B_4 is skewed towards larger sizes compared to the population in sample F-B_{130}, giving a lower number density. A possible cause for this inrease in number density could be interaction between B and (Al,Mg,Si)-nitrides. B is a known nitride former, and research has shown that B can substitute Al in aluminium nitrides (AlN).[46,47] Thus, B could potentially affect the nucleation of (Al,Mg,Si)-nitrides. It is not understood what might cause the number densities of (Al,Mg,Si)-nitrides to differ between the ferritic and mixed grade alloys. Strande *et al.*[48] investigated the formation of hexagonal boronitrides (h-BN) in grey cast iron and how these particles may affect graphite nucleation by acting as heterogeneous nuclei. However, the reseachers were not able to observe these particles in the material using SEM with EDS and WDS, which could indicate such particles are small. This means, if h-BN particles are present in the material in the current study, they are not accounted for as a nitride particle in AMICS due to the 0.5 μm cut-off size used.

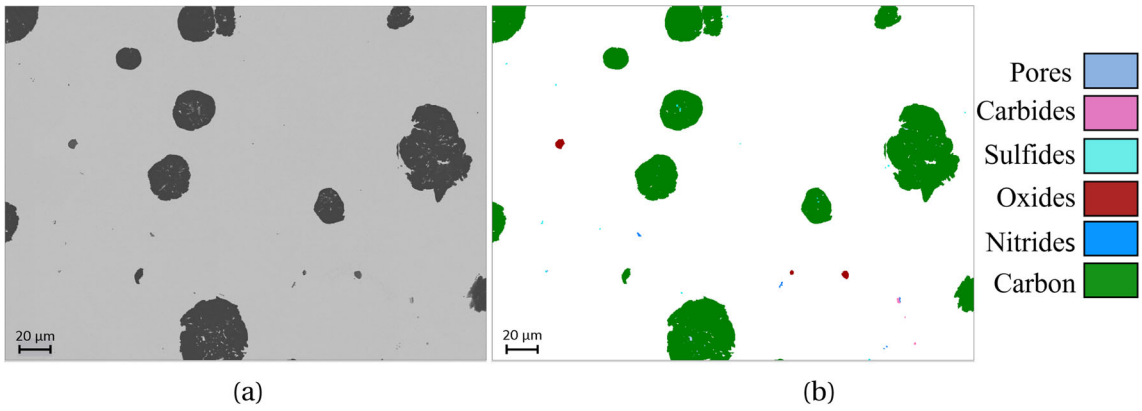

Fig. 9—The BSE image (*a*) of a region within the analyzed area for sample F-B_{130}, and its counterpart where particles have been classified based on EDS (*b*).

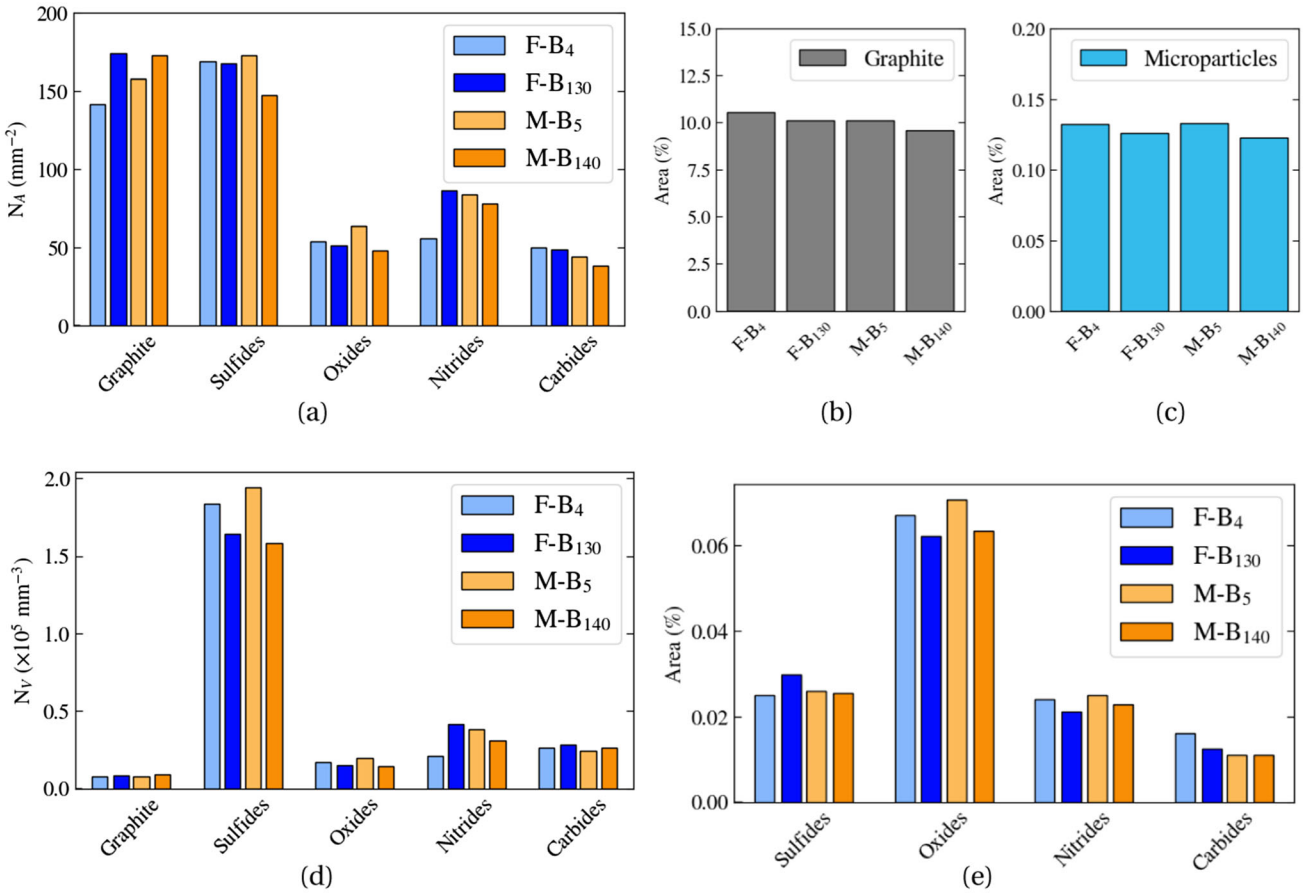

Fig. 10—(*a*) The area number density of graphite nodules and microparticles. (*b*) The area fraction of graphite nodules. (*c*) The total area fraction of microparticles. (*d*) The volume number density of graphite nodules and microparticles. (*e*) The area fraction of microparticles independently.

The increase which can be observed for the graphite particle number density in the ferritic alloys could be a consequence of the increased number density of nitrides. On the contrary, the number densities of sulfides, oxides and nitrides all decrease slightly for the mixed grade alloys. However, the number density of graphite particles for these alloys still increases with increasing B concentration. This suggests that the measured increase in graphite particle number density for the ferritic and mixed grade alloys may be unrelated to the influence of B on the microparticle populations. Further still, there is no concrete results in this study that

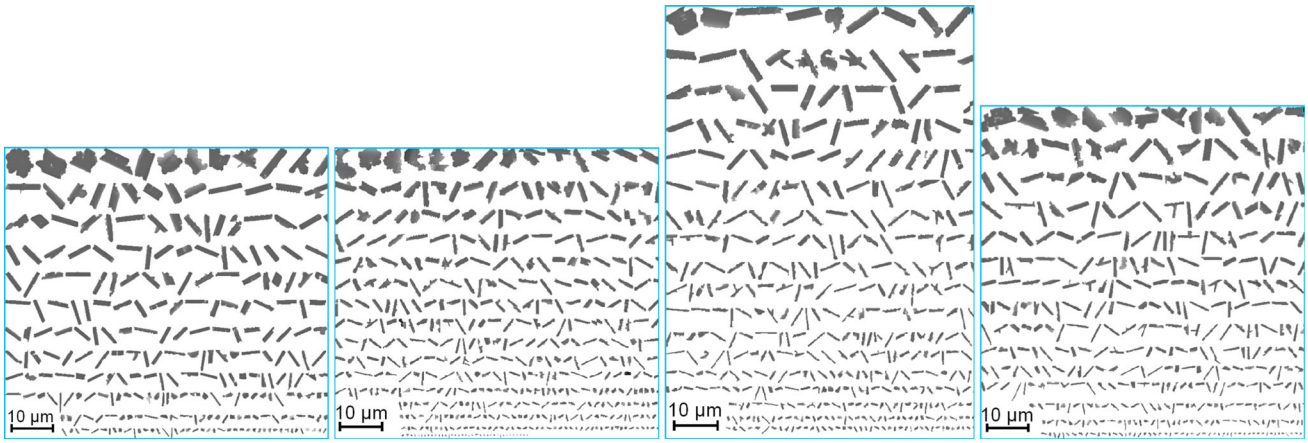

(a) F-B_4 (b) F-B_{130} (c) M-B_5 (d) M-B_{140}

Fig. 11—Nitride particle shapes for the samples of the ferritic (F) and mixed (M) grades investigated with AMICS.

suggests 130 to 140 ppm of B affects the graphite particle number density to a great extent. An explanation of the observed minute increase in nodule number density could very well be unrelated to B. Escobar *et al.*[49] investigated the effects of pouring temperature on nodule number density. The researchers found that a 50 °C lower pouring temperature gave a consistently larger nodule number density due to the faster cooling that occurs when less heat is in the mold. This was investigated both experimentally and by modelling at temperatures of 1250 and 1200 °C. For a mold with thickness 30 mm, it was found that a 50 °C lower pouring temperature led to an increase in nodule number density by approximately 5100 mm^{-3}. Modelling showed, however, a difference in nodule number density of approximately 270 mm^{-3}. In the current study, the high B alloys were poured at a temperature approximately 30 °C lower than the low B alloys. The estimated differences in graphite particle number density between the low B and high B alloys investigated with AMICS were found to be approximately 260 mm^{-3} higher for the high B ferritic alloys than in the low B ferritic alloys. For the mixed grade alloys the estimated graphite particle number density was approximately 1400 mm^{-3} higher for the high B alloy than for the low B mixed grade alloy. Thus, the effect of varying pouring temperature cannot be disregarded when interpreting the results, since it could mask the effect of B. Keeping this in mind, and acknowledging the fact that the differences in graphite particle number density are observed to be small, the results could suggest the influence of 130 to 140 ppm of B on the graphite particle and microparticle number densities is minimal.

In the current study it was checked whether 130 to 140 ppm of B can change the morphology of microparticles by comparing the particle populations visually, similarly to what is presented in Figure 9 for nitride particles, but no such effect was observed. Furthermore, it was not observed any consistent correlation between areas of increased boron concentration and microparticles in the SIMS investigation.

V. CONCLUSIONS

This study investigates the role of boron in spheroidal graphite iron (SGI) using a combination of techniques, including SIMS, microstructure evaluation through OM and SEM, EBSD for phase determination, and quantification of microparticles through an automated SEM/EDS approach.

Optical microscopy techniques revealed that a carbide phase was increasingly formed in the matrix with increasing boron content. Measurements showed constant ferrite and graphite fractions for the investigated boron levels, indicating that the carbide phase grows at the expense of the fraction of pearlite when summing fraction of ferrite, graphite, pearlite and carbide to 100 pct. Additionally, it was observed that the graphite nodule shape began to degenerate when the boron concentration exceeded approximately 300 ppm, resulting in a sharp drop in nodularity. The nodularity was approximately constant for boron concentrations below 300 ppm.

The SIMS analysis indicated the carbide phase contained boron. By performing EBSD of the carbide phase, and comparing the experimentally obtained Kikuchi patterns with simulated patterns, it was determined that the observed carbide phase in an alloy containing 74 ppm boron was $M_{23}(C,B)_6$. According to the SIMS analysis, also V was found in or around this phase. Other elements such as Mn may also be present.

It was also detected elevated concentrations of B in the surface layers of the graphite nodules using SIMS. This could be realted to the rough surface morphology of the nodules observed in the alloys with concentrations of B ranging from 24 ppm to 140 ppm.

No significant changes in the microparticle populations were documented with AMICS for boron concentrations of approximately 130 to 140 ppm. This is in line with the SIMS analysis, which showed no correlation between microparticles and increased boron concentrations. The small increase in graphite particle number densities observed in the AMICS study could not be

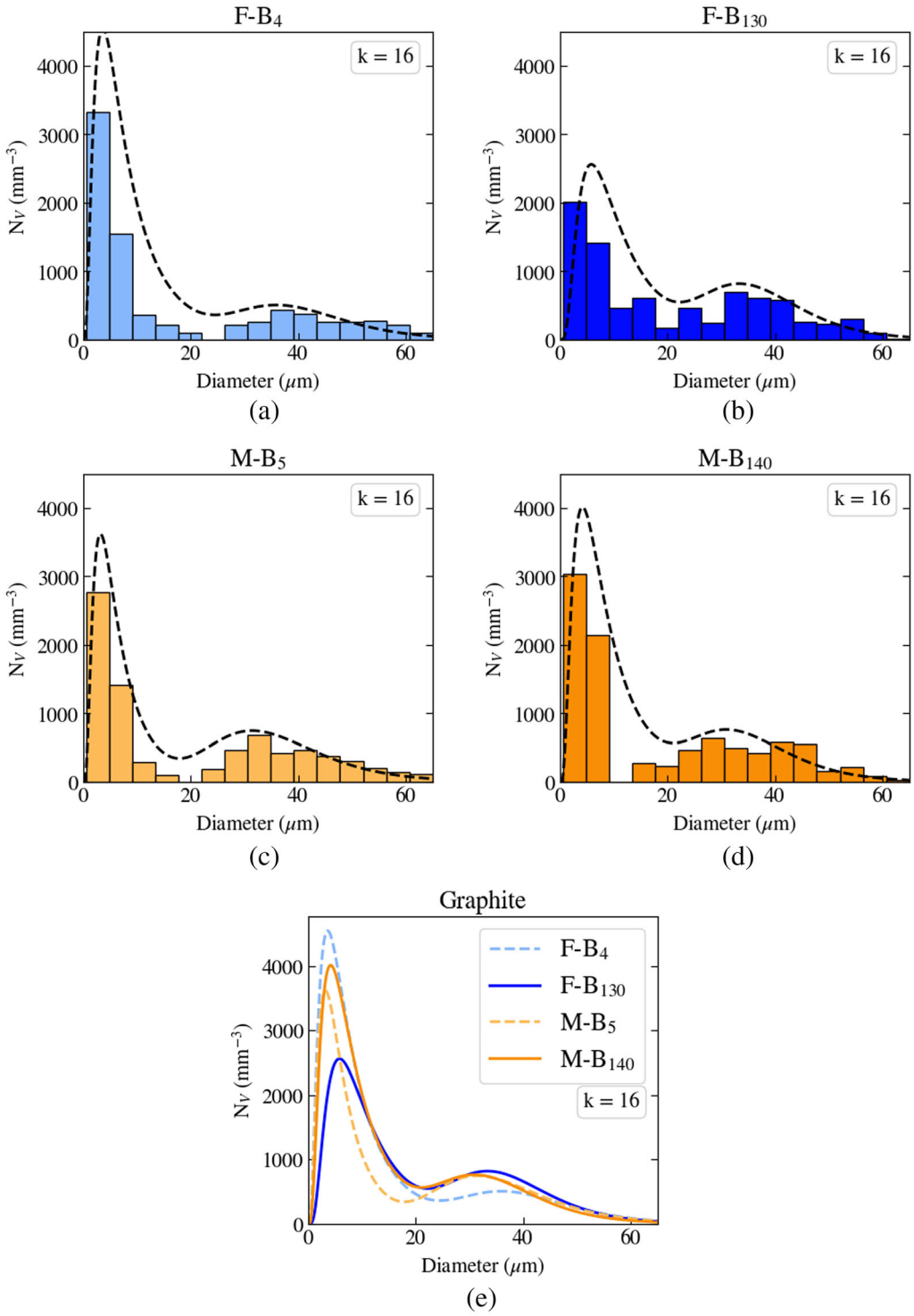

Fig. 12—(*a*)–(*d*) The size distributions for graphite in the various samples. (*e*) The log-normal functions for the distributions.

attributed to the increased B concentration because of the variation in pouring temperature which could mask any potential influence of B. However, taking the varying pouring temperature into account, the results from the AMICS study suggests that the influence of 130 to 140 ppm of B on the microparticle populations is negligible. No significant effect of 130–140 ppm of B could be observed on the size distributions or number densities of graphite nodules.

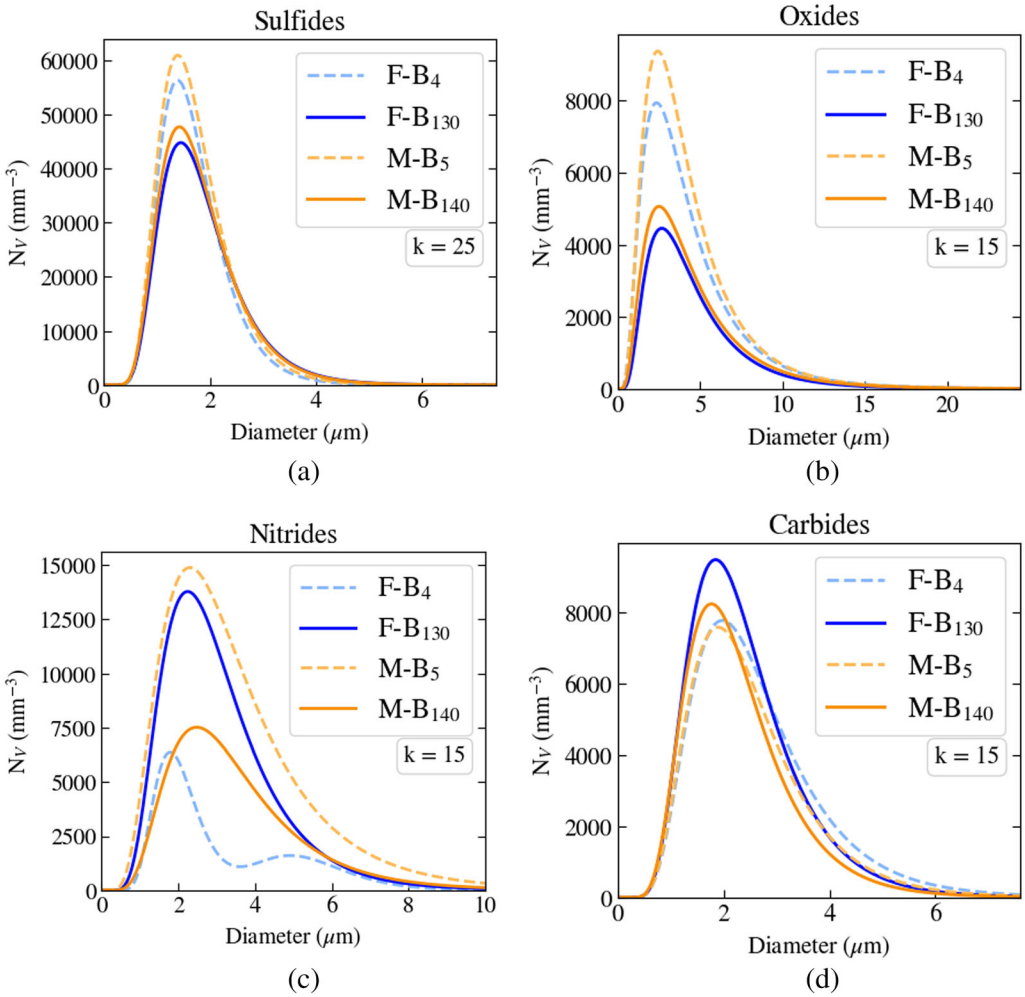

Fig. 13—(*a*)–(*d*) The log-normal functions for the size distributions of sulfide, oxide, nitride, and carbide particles.

ACKNOWLEDGMENTS

This work has been funded by the SFI PhysMet, (Centre for Research-based Innovation, 309584). The authors gratefully acknowledge the financial support from the Research Council of Norway and the partners of the SFI PhysMet. The authors acknowledge Dr. Gro Eide at Elkem Silicon Products for her scientific support. The authors want to thank Bente Kroka at Elkem Silicon Products for the optical microscope and AMICS analyses, and Dr. Eivind G. Hoel at Elkem Silicon Products for the valuable technical assistance and discussions. The authors are grateful to Håkon Wiik Ånes at the Department of Materials Science and Engineering (NTNU) for assisting with kikuchipy and EMsoft. The authors are grateful to James Vaughan at Elkem Silicon Products for suggesting the boron levels.

FUNDING

Open access funding provided by NTNU Norwegian University of Science and Technology (incl St. Olavs Hospital - Trondheim University Hospital).

CONFLICT OF INTEREST

The authors declare that they have no conflict of interest.

REFERENCES

1. D. Venugopalan: *Metall. Mater. Trans. A*, 1990, vol. 21, pp. 913–18.
2. A. Pires, S. Simões, L. Michels, E. Ott, C. Hartung, and C.S. Ribeiro: *Metals*, 2022, vol. 13, pp. 1–19.
3. T. Skaland, Ø. Grong, and T. Grong: *Metall. Mater. Trans. A*, 1993, vol. 24, pp. 2321–45.
4. C. Hartung, M. Liptak, R. Logan, and L. Michels: Int. J. Metalcast., 2023. https://doi.org/10.1007/s40962-022-00947-x.
5. American Foundry Society: *Ductile Iron Handbook*, American Foundry Society (AFS), Des Plaines, 1992, pp.66–99.
6. L. Michels, A.J.F. Pires, C.A.S. Ribeiro, B. Kroka, E.G. Hoel, E. Ott, and C. Hartung: *Metall. Mater. Trans. B.*, 2022, vol. 53, pp. 836–47.
7. S. Hiratsuka, H. Horie, T. Kowata, K. Koike, and K. Shimizu: *Mater. Trans.*, 2003, vol. 44, pp. 1419–24.
8. P. Futáš, A. Pribulová, G. Fedorko, and V. Molnár: *ISIJ Int.*, 2017, vol. 57, pp. 374–9.
9. Z. Glavas: *Kovové Mater.*, 2012, vol. 50, pp. 75–82.
10. E. Billur: *Hot Stamping of Ultra High-Strength Steels*, Springer, Cham, 2019, pp.11–14.
11. G.W. Queirós, L.G. Sanchez, J.M. Gómez de Salazar, and A.J. Criado: *J. Mater. Sci. Eng.*, 2018, vol. 7, pp. 1–4.
12. D.M. Stefanescu: *ASM Handbook: Cast Iron Science and Technology*, vol. 1A, ASM International, Materials Park, 2017, pp.605–30.
13. J. Lacaze: *Int. J. Metalcast.*, 2017, vol. 11, pp. 44–51.
14. R. Voigt: Trace (minor) elements in cast irons, in *ASM Handbook: Cast Iron Science and Technology*, ASM International, Materials Park, 2017, pp.177–81.
15. Y. Zou, M. Ogawa, and H. Nakae: *ISIJ Int.*, 2012, vol. 52, pp. 505–9.
16. K.A. Kasvayee, M. Ciavatta, E. Ghassemali, I.L. Svensson, and A.E.W. Jarfors: *Mater. Sci. Forum.*, 2018, vol. 925, pp. 249–56.
17. S. Izui, N. Furumiya, H. Horie, K. Toshinori, and T. Toshihiko: *Imono*, 1994, vol. 66, pp. 745–05.
18. L.F.V. Guerra, A. Bedolla-Jacuinde, I. Mejía, J. Zuno, and C. Maldonado: *Mater. Sci. Eng. A*, 2015, vol. 648, pp. 193–201.
19. S. Mitra, D. Roy, T. Bhattacharyya, and P.P. Chattopadhyay: *Ironmak. Steelmak.*, 2018, vol. 45, pp. 1–5.
20. Y.C. Peng, H.J. Jin, J.H. Liu, and G.L. Li: *Mater. Sci. Eng. A*, 2011, vol. 529, pp. 321–5.
21. C. Basak: *Scr. Mater.*, 2004, vol. 51, pp. 255–60.
22. H.W. Ånes, L. Lervik, T.B. Onatlandsmyr, Z. Xu, E. Prestat: *Pyxem/kikuchipy: kikuchipy 0.5.8 (v0.5.8), Zenodo*, 2022. https://doi.org/10.5281/zenodo.6554848.
23. Y.H. Chen, S.U. Park, D. Wei, G. Newstadt, M.A. Jackson, J.P. Simmons, M. De Graef, and A.O. Hero: *Microsc. Microanal.*, 2015, vol. 21, pp. 739–52.
24. M.A. Jackson, E. Pascal, and M. De Graef: *Integr. Mater. Manuf. Innov.*, 2019, vol. 8, pp. 226–46.
25. J. Takahashi, and H. Suito: *Metall. Mater. Trans. A*, 2003, vol. 34, pp. 171–81.
26. Y. Gulbin: *Image Anal. Stereol.*, 2011, vol. 27, p. 163.
27. C.W. Bale, E. Bélisle, P. Chartrand, S.A. Decterov, G. Eriksson, A.E. Gheribi, K. Hack, I.-H. Jung, Y.-B. Kang, J. Melançon, A.D. Pelton, S. Petersen, C. Robelin, J. Sangster, P. Spencer, and M.A. Van Ende: *Calphad*, 2016, vol. 54, pp. 35–53.
28. Thermo-Calc Software: *Fe-alloys Database version 12*, 2022.
29. G. Alonso, D.M. Stefanescu, P. Larrañaga, and R. Suarez: *Int. J. CastMet. Res.*, 2016, vol. 29, pp. 2–11.
30. S. Izui, N. Furumiya, H. Horie, T. Kowata, and T. Takahashi: *J. Jpn. Foundrym. Soc.*, 1994, vol. 66, pp. 645–750.
31. M. Reibold, A.A. Levin, D.C. Meyer, P. Paufler, and W. Kochmann: *Int. J. Mater. Res.*, 2006, vol. 97, pp. 1172–82.
32. D. Fruchart, P. Chaudouet, R. Fruchart, A. Rouault, and J.P. Senateur: *J. Solid State Chem.*, 1984, vol. 51, pp. 246–52.
33. Z.F. Zhang, P. Qian, Y.P. Li, J.C. Li, J. Shen, and N.X. Chen: *J. Solid State Chem.*, 2013, vol. 199, pp. 27–33.
34. M.L. Borlera, and G. Pradelli: *La Metall. Ital.*, 1971, vol. 63, pp. 107–11.
35. J. Qing, S. Lekakh, M. Xu, and D. Field: *Carbon*, 2021, vol. 171, pp. 276–88.
36. G. Alonso, T. Tokarski, D.M. Stefanescu, M. Górny, G. Cios, and R. Suarez: *Carbon*, 2022, vol. 199, pp. 170–80.
37. S.N. Lekakh: *Int. J. Metalcast.*, 2020, vol. 14, pp. 1078–89.
38. Y. Igarashi, and S. Okada: *Int. J. CastMet. Res.*, 1998, vol. 11, pp. 83–8.
39. J.K. Solberg, and M.I. Onsøien: *Mater. Sci. Technol.*, 2001, vol. 17, pp. 1238–42.
40. L. Laffont, A. Pugliara, T. Hungria, and J. Lacaze: *J. Mater. Res. Technol.*, 2020, vol. 9, pp. 4665–71.
41. D.M. Stefanescu, A. Crisan, G. Alonso, P. Larrañaga, and R. Suarez: *Metall. Mater. Trans. A*, 2019, vol. 50, pp. 1763–72.
42. J. Lentz, A. Röttger, and W. Theisen: *Mater. Charact.*, 2018, vol. 135, pp. 192–202.
43. H.M. Muhmond, and H. Fredriksson: *Metall. Mater. Trans. A*, 2014, vol. 45, pp. 6187–99.
44. B. Tonn, J. Lacaze, and S. Duwe: *Mater. Sci. Forum.*, 2018, vol. 925, pp. 62–9.
45. D.M. Stefanescu, G. Alonso, P. Larrañaga, E. De la Fuente, and R. Suarez: *Acta Mater.*, 2016, vol. 107, pp. 102–26.
46. E. Viswanathan, M. Sundareswari, S. Krishnaveni, M. Manjula, and D.S. Jayalakshmi: *J. Superhard Mater.*, 2019, vol. 41, pp. 321–33.
47. N.P. Bezhenar, S.A. Bozhko, N.N. Belyavina, and V. YaMarkiv: *Diam. Relat. Mater.*, 1996, vol. **6**, pp. 927–30.
48. K. Strande, N.S. Tiedje, and M. Chen: *Int. J. Metalcast.*, 2017, vol. 11, pp. 61–70.
49. A. Escobar, D. Celentano, M. Cruchaga, and B. Schulz: *Metals*, 2015, vol. 5, pp. 628–47.